Machine Learning Optimization of P-Type Transparent Conducting Films

Lingfei Wei,[†,‡] *Xiaojie Xu,*[§] *Gurudayal,*[‡,⊥] *James Bullock,*[‖] *and Joel W. Ager,*[*,‡,⊥,∇]

† School of Chemistry and Chemical Engineering, Southeast University, Nanjing 211189, P. R. China

‡ Materials Sciences Division, Lawrence Berkeley National Laboratory, Berkeley, CA 94720, United States of America

§ Materials Sciences Division, Lawrence Livermore National Laboratory, Livermore, CA 94550, United States of America

⊥ Joint Center for Artificial Photosynthesis, Lawrence Berkeley National Laboratory, Berkeley, CA 94720, United States of America

‖ Department of Electrical and Electronic Engineering, University of Melbourne, Melbourne, Victoria, Australia

∇ Department of Materials Science and Engineering, University of California Berkeley, Berkeley, CA 94720, United States of America

ABSTRACT

P-type transparent conducting materials (p-TCMs) are important components of optoelectronic devices including solar cells, photodetectors, displays, and flexible sensors. Cu-Zn-S (CZS) thin films prepared by chemical bath deposition (CBD) can have both high transparency in the visible range (>80%) as well as excellent hole conductivity (>1000 S cm^{-1}). However, the interplay between the deposition parameters in the CBD process (metal and sulfur precursor concentrations, temperature, pH, complexing agents, etc.) creates a multi-dimensional parameter space such that optimization for a specific application is challenging and time consuming. Here, we show that strategic design of experiment (DOE) combined with machine learning (ML) allows for efficient optimization of p-TCM performance. The approach is guided by a figure of merit (FOM) calculated from the film conductivity and optical transmission in the desired spectral range. A specific example is shown using two steps of optimization using a selected subset of 4 experimental CBD factors. The machine learning model is based on support vector regression (SVR) employing a radial basis function (RBF) as the kernel function. 10-fold cross-validation was performed to mitigate overfitting. After the first round of optimization, predicted areas in the parameter space with maximal FOMs were selected for a second round of optimization. Films with optimal FOMs were incorporated into heterojunction solar cells and transparent photodiodes. The optimization approach shown here will be generally applicable to any materials synthesis process with multiple parameters.

INTRODUCTION

P-type transparent conducting materials (p-TCMs) have applications as components in a number of electronic devices such as touchscreens, LCD layers, LEDs, and photovoltaics.[1–4] Oxides such as delafossites (e.g., $CuAlO_2$, $CuGaO_2$, $CuInO_2$, etc.)[5], spinels (AB_2O_4, e.g., $NiCo_2O_4$)[6,7], and

mixed oxides (e.g., In_2O_3-Ag_2O)[8] have been investigated as p-TCMs in the past few years,[9] but it has been difficult to obtain the desired combination of high transparency and conductivity. Sulfides have also been investigated as TCMs.[10–16] In particular, the Cu-Zn-S system (CZS) has been the subject of investigation since the first report of p-type behavior in 1999.[17] Although a number of methods can be employed to make thin CZS films including pulsed laser deposition (PLD) and sputtering,[15,18–21] solution based methods such as chemical bath deposition (CBD) are attractive from a scalability point of view.[14,22–28] In our previous work, $(CuS)_x(ZnS)_{1-x}$ nanocomposites were deposited by CBD and found to possess hole conductivity as high as 1000 S cm^{-1} and optical transmission above 70% in the visible range of the spectrum.[29]

In contrast to the vapor-based deposition methods discussed above, it is less straightforward to tune CBD deposition parameters to produce continuous TCMs of the desired conductivity and transparency. As shown schematically in Figure 1a, heterogeneous nucleation on the substrate and homogeneous nucleation in the solution happen simultaneously during CBD. Additionally, subsequent film growth can proceed by either ion-by-ion or by a cluster-by-cluster process in which the clusters formed by homogeneous nucleation deposit on the substrate.[30] The latter case generates films with a nonuniform surface and large grain sizes, leading to poor substrate adhesion and lower optical transmission (lower part of Figure 1a). To form adherent films, nucleation should happen directly on substrate followed by a moderate rate of ion-by-ion growth (upper part of Figure 1a).[30,31]

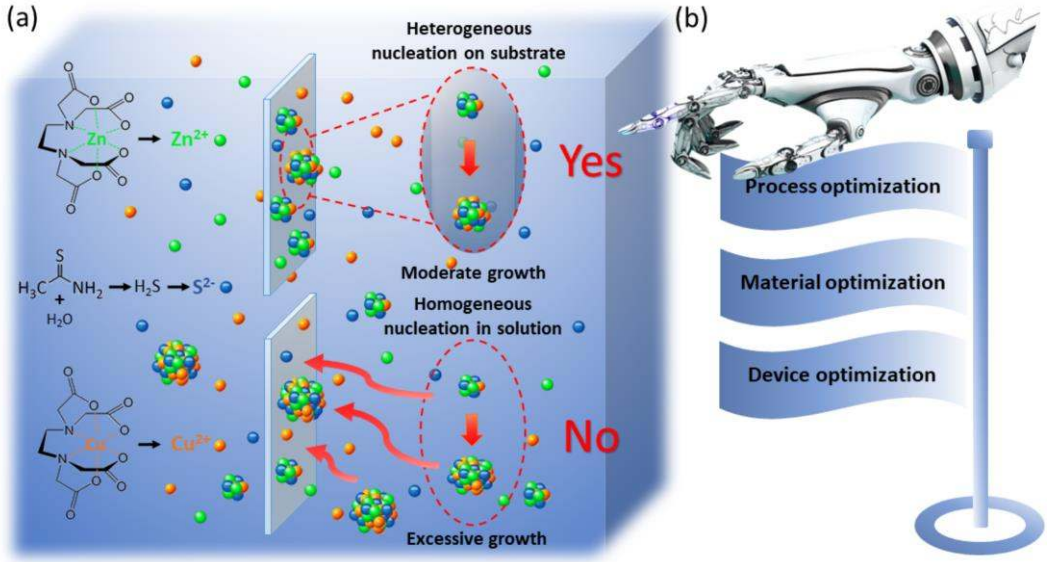

Figure 1. (a) Schematic illustration of the growth mechanisms of $(CuS)_x$:$(ZnS)_{1-x}$ films via chemical bath deposition. Orange, green and blue balls represent Cu^{2+}, Zn^{2+} and S^{2-}, respectively. The upper case depicts heterogeneous nucleation and growth on the substrate. (b) Aims of machine learning optimization in this work. Royalty-free graphic of the robotic hand was obtained from pngtree.com.

There are a number of interrelated process parameters in CBD which will influence the growth mode of $(CuS)_x(ZnS)_{1-x}$ nanocomposite thin films. The first is the relative ratios of the Cu and Zn precursors. Bulk CuS is p-type semiconductor material with a direct band gap of ~2.5 eV,[32] and ZnS is n-type semiconductor material with a direct band gap of ~3.6 eV.[33] The hole conductivity of $(CuS)_x(ZnS)_{1-x}$ nanocomposite films is attributed to the conducting network formed by covellite CuS nanocrystals while the transparency is dependent on the transparent fillers (ZnS) and average nanocrystal sizes.[29] Thus the Cu and Zn precursor ratio will influence the overall optical band gap of the composite, with higher Zn ratios increasing the effective band gap. Higher Cu ratios will

lower the energy band gap but also increase the proportion of the hole-conducting covellite CuS phase. Secondly, the concentration of the complexing agent (Na_2EDTA in our case) affects the crystallite size in two ways. It reduces the aggregation of metal ions and forms a concentration profile of metal ions which is more favorable to nucleation rather than crystal growth. [34,35] At the same time, a high concentration of complexing agent can be undesirable; additional Na_2EDTA can accelerate the growth rate and promote the cluster-by-cluster process, which results in poor quality deposition and nonuniformity.[36] Thirdly, the rate of both nucleation and growth are sensitive to temperature.[37] Finally, the reaction time influences the thickness and quality of CZS thin films. CBD is a self-limiting process with the growth rate declining as the concentration of precursors decreases.[38] In the case of TCM films, the sheet resistance would decrease with increasing film thickness at fixed film conductivity. But if lower quality material (less transparent or less conductive) would be deposited late in the growth cycle, extended reaction times would not be beneficial.

In spite of this complicated reaction environment and multi-dimensional parameter space, we note that most prior studies of this materials system, including our own, have employed a low-efficiency "one factor at a time" approach to optimizing p-TCM properties. We thus hypothesized that a more efficient approach would be to use a more strategic design of experiment guided by a regression model. We note recent examples of machine learning (ML) in materials sciences,[39–42] with a number of studies using a combination of first principles theory and experiment for materials discovery.[43–48] For navigation of a multi-dimensional materials synthesis space, we were inspired by recent studies of machine learning regression models applied to organic electronics.[49,50]

Here, we present a machine learning approach to efficiently optimize p-TCMs within the multi-dimensional parameter space for the CBD process. We use a strategic design of experiment (DOE)

to reduce the number of required experiments. We chose an ML model, support vector regression (SVR), which yields reliable predictions over our parameter space after cross validation. After two rounds of optimization using this approach, an optimal process for transparent (average visible transmittance, AVT, up to 80% at wavelength of 380-780 nm) and conductive (430 S cm^{-1}) CZS films was identified. We then compared the ML-optimized and non-optimized thin films as components of heterojunction solar cells and transparent photodiodes, with the optimized films producing superior behavior in both types of devices as expected. The approach illustrated here is generally applicable to any material synthesis process or materials/devices optimization process and can significantly advance the rate of materials/devices development.

EXPERIMENTAL METHODS

Chemical bath deposition. CZS thin films were synthesized via CBD at solution temperatures between 60 and 90 ºC. Substrates (soda lime glass, silicon and FTO glass) were cleaned sequentially in an ultrasonic bath with detergent, methanol, and deionized water (DIW). The metal precursor solutions were prepared with $CuSO_4$ (purity 99%, Alfa Aesar) and $Zn(CH_3COO)_2$ (99.9%, Alfa Aesar) at a total metal ion concentration of 0.1 M (100 ml). The complexing agent Na_2EDTA (99.9%, Alfa Aesar) solution (50 ml) was adding into the above mixture and thoroughly mixed in an ultrasonic bath for 20 min. Prior to CBD, the growth solution was transferred to a hot plate under constant stirring and heated to, and maintained at, the desired temperature. The growth substrate was suspended vertically in the solution, and deposition was initiated by mixing in 20 ml of the sulfur precursor (0.1 M C_2H_5NS (99.9%, Alfa Aesar). During the reaction, the beaker was covered to limit water evaporation. After the desired growth time (30-120 minutes), the substrate was removed and rinsed with DIW. The obtained samples were cut into desired size for further characterization.

P-TCM characterization. Films thickness were obtained from an average of 20 AFM scans at different positions over a step defined by a shadow mask. Additional thickness measurements were performed with Rutherford backscattering spectrometry (RBS), using a 2 MeV He ion beam, and were simulated with the average atomic density as described previously.[19][29] Surface roughness and morphology were determined by Atomic force microscopy (AFM) in tapping mode using a Veeco-DI equipped with a Nanoscope IV Controller and a silicon tip from ULTRASHARP. The tip has a radius of curvature less than 10 nm, a height of 15 μm, a resonant frequency of 325 kHz, and a force constant of 40 N/m. The camera and photodetector were aligned before each scan, and the tip resonance frequency was tuned using Auto mode. Each measurement was done with a scan size of 1×1 μm^2 and a scan rate of 0.2 Hz. The obtained images were processed with Gwyddion software. UV-vis transmittance and reflectance spectra of samples were obtained using a Lambda 950 UV-vis spectrometer. Room temperature conductivity, mobility, and carrier concentration were measured using the van der Pauw contact configuration with an Ecopia HMS-3000 Hall Measurement System equipped with a 0.55 T magnet.[19] The room temperature Seebeck coefficients were measured by a home-built thermopower system[51,52] (setup details are in Supporting Information) equipped with Keithley 2000-20 multimeter and Lakeshore 331 temperature controllers. All CZS films were p-type as evidenced by positive Hall and Seebeck coefficients.

Design of experiments and p-TCM figure of merit.

While the most commonly used DOE strategy is the so-called two-level factorial design,[53–56] in which only two levels are used for each factor, we chose to use more levels for some of the factors. Our prior work provides guidance for two of the factors, the Cu/Cu+Zn ratio and the Na_2EDTA concentration.[29] As shown in Figure S2a, Cu precursor contents, (Cu/(Cu+Zn), lower than 0.65 or

greater than 0.85 produce films with poor FOMs. This is understandable, as the hole conduction is due to the CuS in the composite structure but a tradeoff exists because this phase is more strongly absorbing in the visible than ZnS. We also showed, Figure S2b, that Na_2EDTA concentrations greater than 0.1 M produce films with large grain sizes and poor transparency. This prior knowledge allowed us to bound the Cu precursor concentration with two levels, 0.65 and 0.85 in the first round of experiments. As we desired greater resolution with the Na_2EDTA concentration, we used 4 levels between 0.20 and 0.1 M. As we had not thoroughly investigated the effect of deposition temperature and time in our prior work, we selected wide ranges for these parameters, 60-90 ºC and 30-120 minutes. It is worth noting the deposition rate of the CBD process is not linear in time, as the rate slows as the precursor are consumed. Thus the choice of 4 levels for this variable will aid in discerning effects which might occur as the growth mechanism changes due to varying reaction conditions. Varying all the parameters independently would necessitate 128 experimental conditions. As repeat experiments are required to establish reproducibility, the full experimental design is clearly too time consuming.[57]

We considered first the three factors with 4 levels. Varying all factors would necessitate 4^3 = 64 experiments. Instead we reduced the design to 16 sets by a 1/4 Generalized Subset Design (GSD).[53,56] We found the oa.design function in the DoE.base package in the open source statistical program R to be useful in constructing a balanced and orthogonal design, as shown in Table 1 and schematically in Figure S3. By duplicating the design on both Cu/(Cu+Zn)=0.65 and 0.85, 32 sets will be generated in our [2,4,4,4] parameter space, with orthogonality achieved within a given Cu/(Cu+Zn) value. Table 1 shows the actual design of 32 sets and 105 data points with repetitions.

Table 1. Experimental conditions and results from the first round DOE (105 experiments including repetitions). FOMs are calculated using the average visible transmission from 380-780 nm and are shown as mean values for each condition.

Set#	Cu/(Cu+Zn)	Temperature (°C)	Time (min)	Concentration of Na_2EDTA (M)	FOM (μS)	Number of samples
1	0.65	60	30	0.02	138	3
2	0.65	60	60	0.03	178	3
3	0.65	60	90	0.07	110	3
4	0.65	60	120	0.1	148	3
5	0.65	70	30	0.03	193	3
6	0.65	70	60	0.07	184	3
7	0.65	70	90	0.1	18.2	3
8	0.65	70	120	0.02	32.8	3
9	0.65	80	30	0.07	54.0	3
10	0.65	80	60	0.1	35.2	3
11	0.65	80	90	0.02	72.0	3
12	0.65	80	120	0.03	62.9	3
13	0.65	90	30	0.1	14.8	3
14	0.65	90	60	0.02	101	3
15	0.65	90	90	0.03	120	4
16	0.65	90	120	0.07	58.1	4
17	0.85	60	30	0.02	31.0	4
18	0.85	60	60	0.03	103	4
19	0.85	60	90	0.07	54.4	4
20	0.85	60	120	0.1	33.9	4
21	0.85	70	30	0.03	80.4	3
22	0.85	70	60	0.07	24.9	4
23	0.85	70	90	0.1	11.0	3
24	0.85	70	120	0.02	32.0	3
25	0.85	80	30	0.07	20.7	3
26	0.85	80	60	0.1	30.2	3
27	0.85	80	90	0.02	81.9	3
28	0.85	80	120	0.03	51.1	3
29	0.85	90	30	0.1	12.2	4
30	0.85	90	60	0.02	125	3
31	0.85	90	90	0.03	149	3
32	0.85	90	120	0.07	14.1	4

Figures of Merits (FOMs), e.g. *ZT* for thermoelectrics, are commonly used in engineering to evaluate the applicability of a materials with different underlying properties.[20,58,59] In this study, we applied an FOM for transparent conductors proposed by Haacke,[60]

$$\Phi_{TC}=T^{10}/R_s \quad (1)$$

The exponent of *T* in Eq. (1) weights the importance of optical transmission vs. electrical conduction for a given application; where *T* is the transmission at a given wavelength or over a wavelength range (AVT at 380-780 nm in this work) and R_s (Ω/□) is sheet resistance.[20,60] The exponent of *T* in Eq. (1) weights the importance of optical transmission vs. electrical conduction for a given application; a larger value of the exponent places greater relative weight on transmission. We chose a value of 10 to provide consistency with previous studies targeting optically transparent devices.[61] For comparison to the values obtained in this study, figure of merits for p-TCM films compiled from the literature (0.002-174 μS) are listed in Table S1.

Machine learning training model. There are a number of choices for a machine learning regression modeling including Linear Regression, Logistic Regression, K-Nearest Neighbors (KNN), Random Forest, etc.[62,63] However, the so-called "no free lunch" theorem states that no algorithm is suitable for every problem and every dataset,[64] such that the choice applicable here to a multi-parameter synthesis space merits discussion. As might we expect correlations and non-linear dependencies, a linear regression model would not be appropriate. Similarly, logistic regression assumes that factors are independent from each other thus is also inapplicable.[65] KNN makes predictions by searching through the entire training set for the most similar neighbors and is most often used for estimating continuous variables. Examination of Table 1 shows that the FOMs in our case hardly follow a simple "continuous" pattern, thus making KNN regression unsuitable in this work.[66] Random forest, one of the most popular regression algorithms in ML,

uses bootstrap aggregation and a random subspace method.[67,68] However, there is a risk of overfitting, and this approach typically does not do well when extrapolation outside of the range of variables is required.

In this work, we employed support vector regression (SVR) implemented with Scikit-learn, a popular ML library for the Python programming language.[69] There are a number of different kernel functions which can be employed including linear, nonlinear, polynomial and sigmoid. We selected the radial basis function (RBF) kernel, as it would be expected to fit the Gaussian-shaped features that would normally be found in cases of optimization.[70–72] As discussed in detail below, a 10-fold cross validation scheme was applied to mitigate against overfitting and artificially high statistics (unreliable statistic results from sampling).[73] More details can be found in the Supporting Information, along with the Python codes we employed.

Device fabrication and measurement. Proof-of-concept p-CZS/n-Si, p-CZS/np$^+$-Si heterojunction solar cells and p-CZS/n-ZnO photodiodes were fabricated to demonstrate the improved device performance using optimized films. For the solar cells,[29] dot contacts were made by electron-beam evaporating Cu/Au (4 nm/60 nm) on the CZS film, while liquid InGa was smeared on the scratched rear surface on n-Si and np$^+$-Si as the back contact. For the photodiodes,[74] CZS films were deposited on FTO glasses via two steps of CBD processes, followed by six layers of n-ZnO deposited by sol-gel spin coating. Each coating of ZnO was followed by an annealing process (300 ^{o}C for 2 min) on a hot plate to evaporate the organic solvent. Dot contacts were made by electron-beam evaporating 60 nm of Au on ZnO surface. The performance of the devices was analyzed by light and dark current density-voltage (*J-V*) measurements using a standard solar simulator (Xe lamp, Solar Co.) under AM 1.5G irradiation (100 mW cm^{-2}) and in the dark. Histograms are used

to show counts for number of devices with different performance.[75,76] Results were fitted with Gaussian amplitude function in Origin. All devices are with an area of 1×1 cm^2.

RESULTS & DISCUSSION

First round statistics. Observed FOMs for the CBD p-TCM films ranged from 11 to 193 μS and were reproducible at a given experimental condition, as shown in the box plot in Figure 2. Analysis of variance (ANOVA) was employed to determine the relative influence of each of the 4 factors on the observed FOM. The p-values for all factors were small, showing that all the factors influence the FOM of the films (Table S2). Figure 3 compares the fraction of the total variance associated with each factor (the residual variance, see Table S2, is not included such that the contributions add to 1). It can be seen that Cu/(Cu+Zn) and the Na_2EDTA concentration are the most influential factors while the process temperature and time contribute approximately equally, but to a lesser degree. As a result, we will use all 4 parameters in the subsequent machine learning regression and in the second round of optimization.

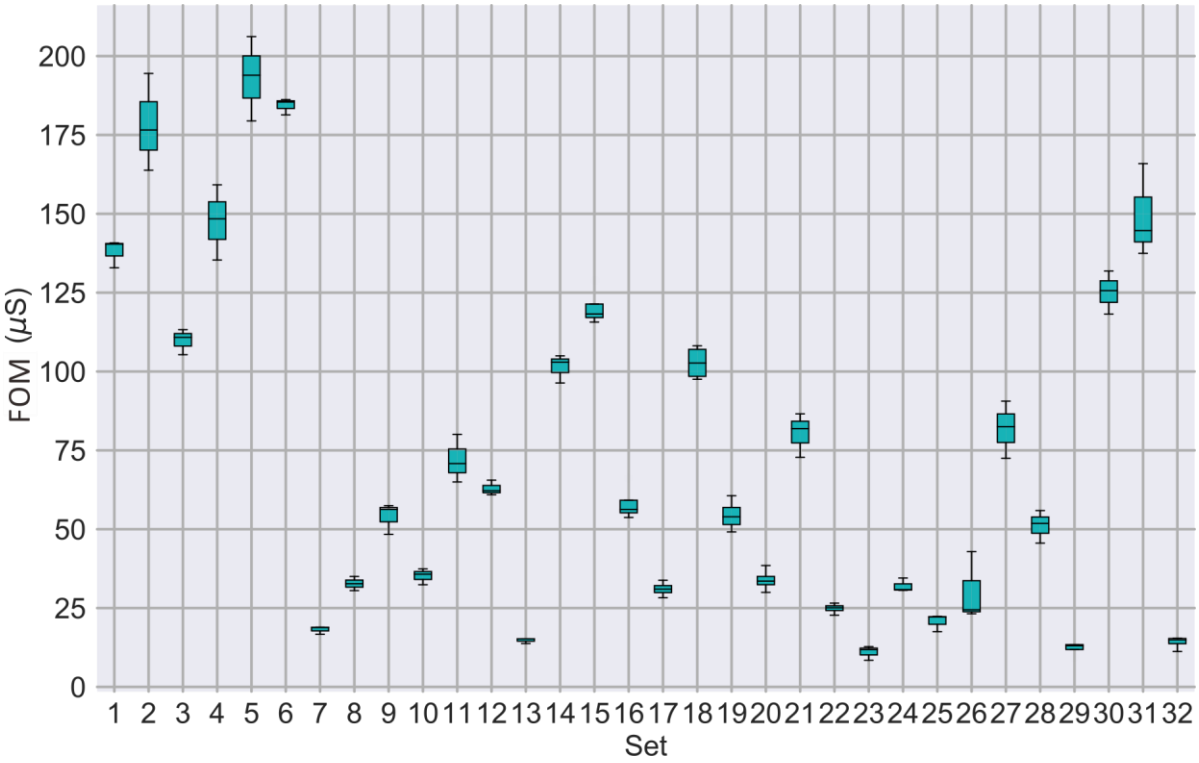

Figure 2. Boxplot of FOMs grouped by set from the first round DOE.

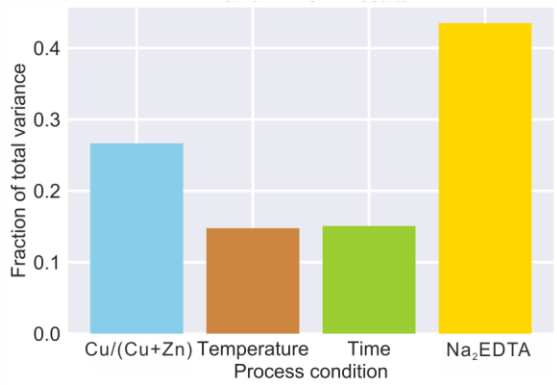

Figure 3. Analysis of variance and factor evaluation from the first round DOE.

Cross validation and first round optimization. Support vector regression (SVR) models with a radial basis function (RBF) employs a kernel function of the form: [77–80]

$$K_{RBF}(\mathbf{x},\mathbf{x'}) = \exp[-\| \mathbf{x}-\mathbf{x'}\|^2 / 2\sigma^2]. \quad (2)$$

In Eq. (2), the independent variables $\boldsymbol{x}$ are the three factors, Cu/(Cu+Zn), reaction time and concentration of Na_2EDTA, while the dependent variable (K_{RBF}) is corresponding FOM. It is important to consider the values of several hyperparameters: ε specifies the epsilon-tube within which no penalty is associated in the training loss function and thus determines support vectors (details can be found in Supporting Information); C, the so-called penalty coefficient of SVM, determines tolerance level for errors; finally, γ ($\gamma=1/2\sigma^2$) defines how far the influence of a single training example reaches. Large C and γ values result in overfitting while small C and γ values lead to underfitting.[81,82] Overfitting happens when a ML model overemphasizes the data on which it was trained and therefore loses its applicability to other datasets. Underfitting happens when a ML model fails to accurately capture relationships between a dataset's parameters and its target variable.

We thus employed 10-fold cross validation to choose optimal values for hyperparameters. The input data were randomly partitioned into 10 equal sized subsamples: 9 subsamples were used as training data, the remaining one as validation data for testing model. The cross validation then repeat for 10 times, with each subsample is used exactly once as the validation data.[83] Testing results are evaluated by mean-squared-error (MSE)[84] in the regression problem, where the smaller MSE is expected for better fitting. Both the input variables (parameters) and output variables (FOMs) were preprocessed to have a mean of zero and a standard deviation of one; [69] This step is necessary when the input variables have different scales. Cross validation learning curves for hyperparameters, scored by the MSE as mentioned before,[85] are shown in Figure 4. In Figure 4a, the red line corresponds to the loss for the training data as γ is increased from 0 to 1.0; the loss remains constant for $\gamma > 0.1$. The minimum loss for the cross-validation data (green line) occurs near γ=0.5, indicating the possibility of overfitting when γ is too small (for example: γ=0.13) or

too large (for example: γ=1). Figure 4b mostly shows a flat trend for both the training and cross validations sets although it can be seen that C < 2 is unacceptable. In Figure 4c, increased ε leads to increasing loss for both training and cross validation. Considering the losses for both the training and cross validations set as well as ML conventions, γ=0.5, C=40 and ε=0.1 were ultimately selected to provide an acceptable balance between under and overfitting.[86]

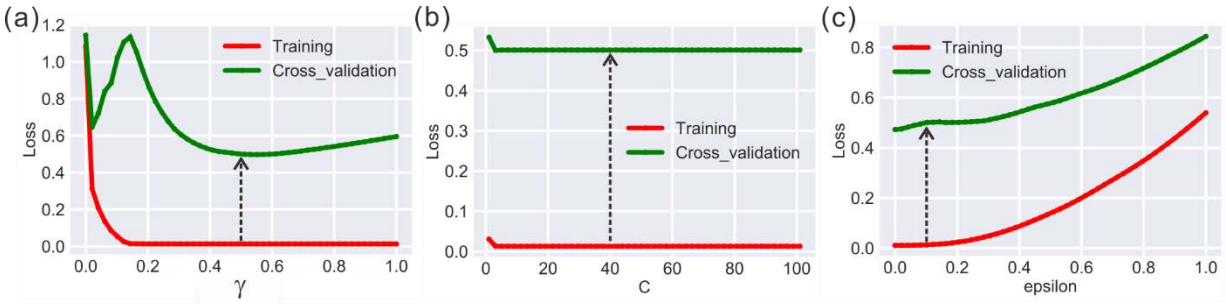

Figure 4. Learning curves from training and cross validation process based on (a) γ (when C=40 and epsilon=0.1); (b) C (when γ=0.5 and epsilon=0.1); (c) epsilon (ε, when γ=0.5 and C=40) using normalized data. Loss is defined as mean squared error (MSE). Black arrows indicate the best choice in each case.

Using hyperparameters discussed above, the first round fitting results are shown in Figure 5a, indicating a good agreement between the SVR model and the experimental data. The dashed line represents equal measured (x-axis) and predicted (y-axis) FOMs. Figure 5b shows that low and high FOMs are approximately equally well predicted with most values lying within a range of $\pm$ 20%.

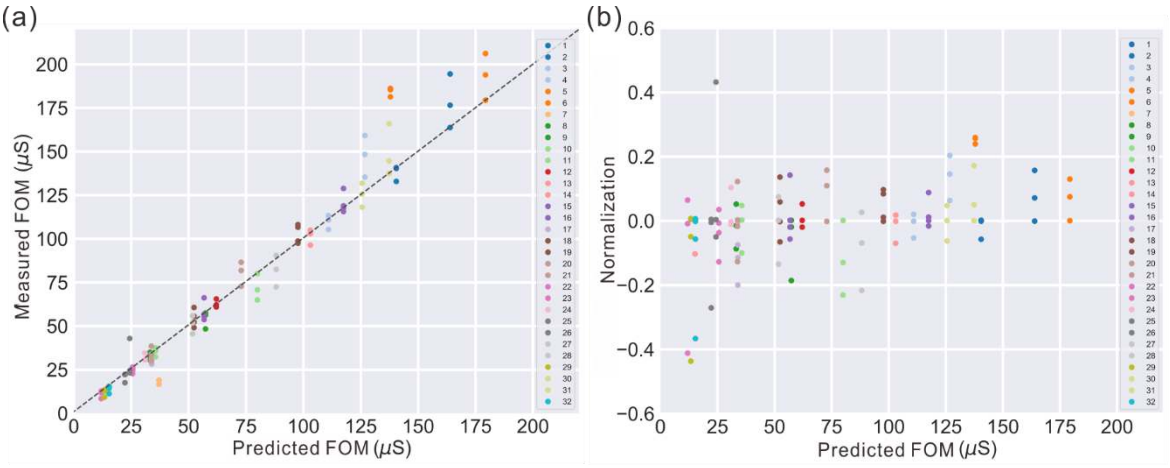

Figure 5. Support vector regression applied to the first round (a) Measured versus predicted FOM and (b) Normalized results versus predicted FOM.

The SVR model can be used to create a three-dimensional map to predict the FOM at any point within the sampled synthesis space. To aid visualization, data is sorted by Cu/(Cu+Zn) and reaction temperature, producing subplot figures at different Cu/(Cu+Zn) and reaction temperature levels, with reaction time as the x axis and the concentration of Na_2EDTA as the y axis (Figure 6). The color gradient, scaled as indicated by the color bar on the right, and the contour lines map out how FOM changes with different reaction time and concentration of Na_2EDTA.[49] It is immediately apparent that higher FOMs come from films with Cu/(Cu+Zn)=0.65, which may be due to the high weight given to transmission (exponent=10) when calculating FOM (eq. (1)). An exception can be found when temperature=90 ^oC, where Cu/(Cu+Zn)=0.85 provides possibilities of higher FOMs. Also, higher FOMs are achieved with lower Na_2EDTA concentrations at all temperatures and Cu contents. Shorter reaction times are needed for high FOMs at lower temperature (60-80 ^oC) and Cu content, but the relationship is more complex for other conditions. In general, the highest FOMs can be obtained at Cu/(Cu+Zn)=0.65 under 70 ^oC, with lower Na_2EDTA concentration and shorter reaction times.

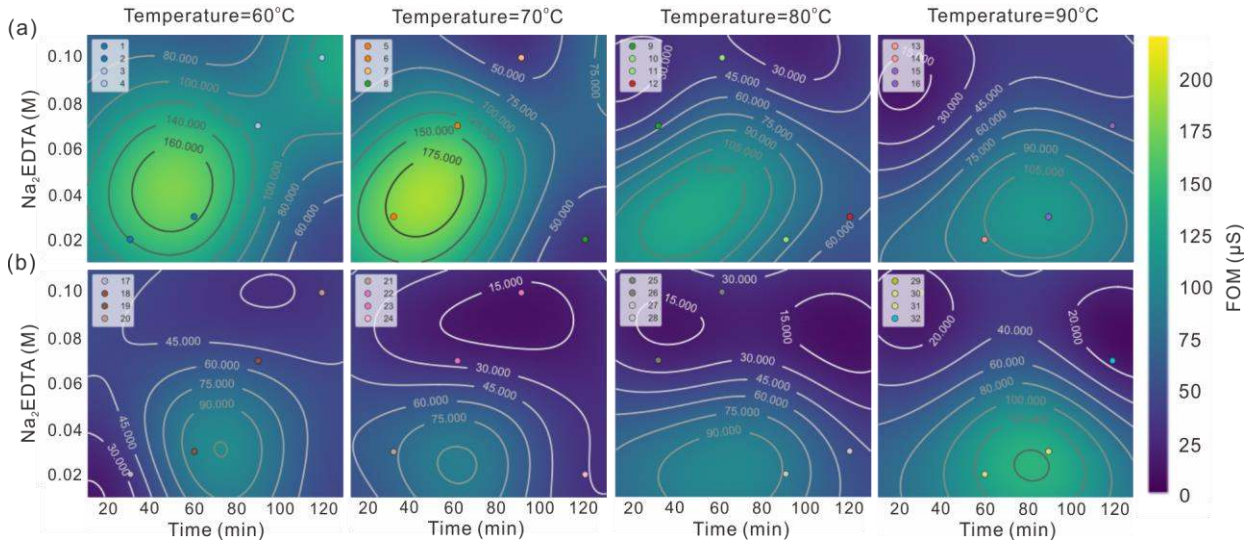

Figure 6. Contour maps of predicted FOMs as a function of deposition time and Na_2EDTA concentration from the first round:(a) Cu/(Cu+Zn)=0.65 and (b) Cu/(Cu+Zn)=0.85. FOM scale and contours were chosen to emphasize the full range of the predicted FOMs.

Relating the results to the CBD process, higher Cu/(Cu+Zn) produces better conductivity but decreases the transparency. The definition of FOM in Eq. (1) emphasizes transparency, thus films with Cu/(Cu+Zn)=0.65 yield higher FOMs in general. It is also interesting that high FOMs are mostly obtained with shorter reaction times. In our previous work, the film growth rate slowed after 60 min;[29] it appears to be the case that longer reaction times cause poor quality growth on the surface, which negatively influences both film conductivity and transparency. Also, FOMs decrease with higher Na_2EDTA concentrations, which may because of poor film quality and nonuniformity,[36] as will be revealed by AFM, discussed below.

Data evaluation and second round optimization. Based on results from the first round of optimization, the range of factors can be further narrowed. Observing that FOMs less than 100 μS are obtained with high temperature, Cu content and Na_2EDTA concentration, we excluded parameter spaces in these ranges. Reaction time was narrowed in the range 40-70 min while Cu

content was studied at around Cu/(Cu+Zn)=0.65. For this round, all 4 parameters were varied over 3 levels. A full [3,3,3,3] design would require 3^4=81 experiments. Instead, a 1/3 GSD with balanced and orthogonal sampling was used to select 27 experiments, Table 2.

Table 2. Experimental conditions and results from the second round DOE (92 experiments including repetitions). FOMs are calculated using the average visible transmission from 380-780 nm and are shown as mean values for each condition.

Set#	Cu/(Cu+Zn)	Temperature (°C)	Time (min)	Concentration of Na_2EDTA (M)	FOM (μS)	Number of samples
1	0.6	60	50	0.05	102	4
2	0.6	60	60	0.03	8	3
3	0.6	60	70	0.04	110	4
4	0.6	70	50	0.03	175	3
5	0.6	70	60	0.04	158	3
6	0.6	70	70	0.05	86.0	3
7	0.6	80	50	0.04	123	4
8	0.6	80	60	0.05	104	4
9	0.6	80	70	0.03	150	3
10	0.65	60	50	0.05	110	3
11	0.65	60	60	0.03	178	3
12	0.65	60	70	0.04	125	3
13	0.65	70	50	0.03	216	3
14	0.65	70	60	0.04	184	3
15	0.65	70	70	0.05	90.0	4
16	0.65	80	50	0.04	140	4
17	0.65	80	60	0.05	110	3
18	0.65	80	70	0.03	155	4
19	0.7	60	50	0.05	102	4
20	0.7	60	60	0.03	118	3
21	0.7	60	70	0.04	114	3
22	0.7	70	50	0.03	133	4
23	0.7	70	60	0.04	95.9	3
24	0.7	70	70	0.05	91.8	3
25	0.7	80	50	0.04	157	3
26	0.7	80	60	0.05	102	4
27	0.7	80	70	0.03	192	4

As with the first round, reproducibility at a given condition was very good, as illustrated by the box plot in Figure S4. Over this parameter range, ANOVA (Figure S5) showed that reaction temperature, reaction time and Cu content do not contribute much to FOMs, while Na_2EDTA concentration significantly influences FOMs, even in a small range. Considering that the second round were generated from the first found optimization, the same hyperparameters were applied here (C = 40 and γ = 0.5 and ε = 0.1). As shown in Figure S6, the model fits the data well and without apparent bias, with most values predicted to within a range of $\pm$10%. Figure 7 shows contour maps sliced from the three levels of Cu/(Cu+Zn) and of reaction temperature. The analysis allows a few observations to be made. (1) The optimized parameter space from first round gives FOMs greater than 100 µS for each of the Cu/(Cu+Zn) and temperature levels, albeit with different deposition times and Na_2EDTA concentrations, indicating the effectiveness of the first round DOE; (2) Highest FOMs (>210µS) seems to be obtained with reaction time of 50-60 min and Na_2EDTA concentrations of 0.03-0.04 M, at Cu/(Cu+Zn)=0.65. However, this is not commonly applicable in other cases, as longer reaction times (~70 min) also give FOMs as high as 192 µS. As indicated by ANOVA, reaction time, temperature and Cu content do contribute less to FOMs in the narrowed parameter space, while Na_2EDTA concentration remains the primary influential factor even with the narrowed space; (3) Na_2EDTA concentrations has a large effect on FOMs, with ~0.03 M exhibiting higher FOMs, which is consistent with a more uniform (and small) crystals, as shown below.

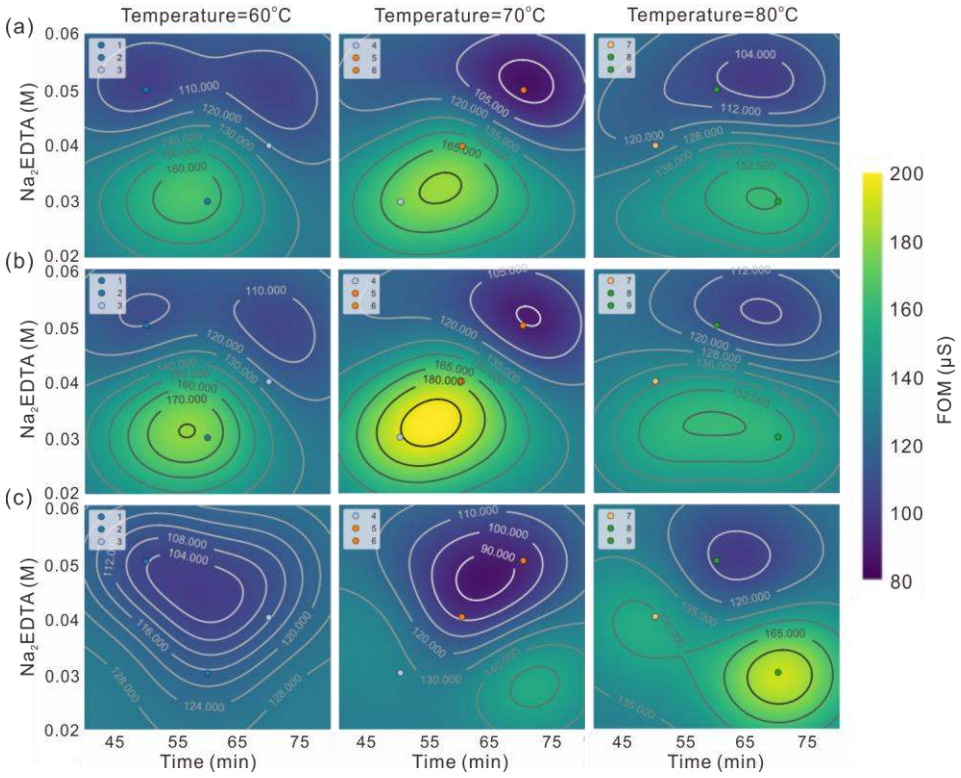

Figure 7. Contour maps of predicted FOMs as a function of deposition time and Na_2EDTA concentration from the second round:(a) Cu/(Cu+Zn)=0.60, (b) Cu/(Cu+Zn)=0.65 and (c) Cu/(Cu+Zn)=0.70. FOM scale and contours were chosen to emphasize the full range of the predicted FOMs.

Comparison to literature reports. Table S1 tabulates calculated FOMs (using Eq (1)) of p-TCMs deposited via different methods including pulsed laser deposition, sputtering, spray pyrolysis, and CBD. Values obtained here from two rounds of optimization compare well to reports of Cu-Zn-S and Cu-Al-S made by CBD and sputtering.

Optical properties and surface imaging. Two conditions were selected from SVR optimization as optimized and non-optimized thin films for further analysis. Table 3 gives the reaction conditions and film performance for them. A higher AVT (Figure 8a) and lower sheet resistance

are exhibited by the optimized film, thus yielding an excellent FOM. The Tauc plot in Figure 8b indicates that the band gaps of the two film are 2.9 and 2.6 eV, respectively. AFM images in Figure 8c and d show a uniform surface with homogeneous distributed small particles for the optimized film (R_q=7.2, indicating a small surface roughness), while the non-optimized film has a nonuniform surface with scattered large particles (R_q=11.9).

Table 3. Comparison of optical and electrical properties for optimized and non-optimized films. AVT, Sheet resistance and FOM are mean values of 10 samples with the same reaction condition.

Film	Cu/(Cu+Zn)	Temperature (°C)	Time (min)	Con. of Na_2EDTA (M)	AVT (380-780 nm, %)	Sheet resistance (Ω/□)	FOM (μS)
Non-optimized	0.85	80	60	0.1	0.57	529	14.8
Optimized	0.65	70	60	0.03	0.75	363	173

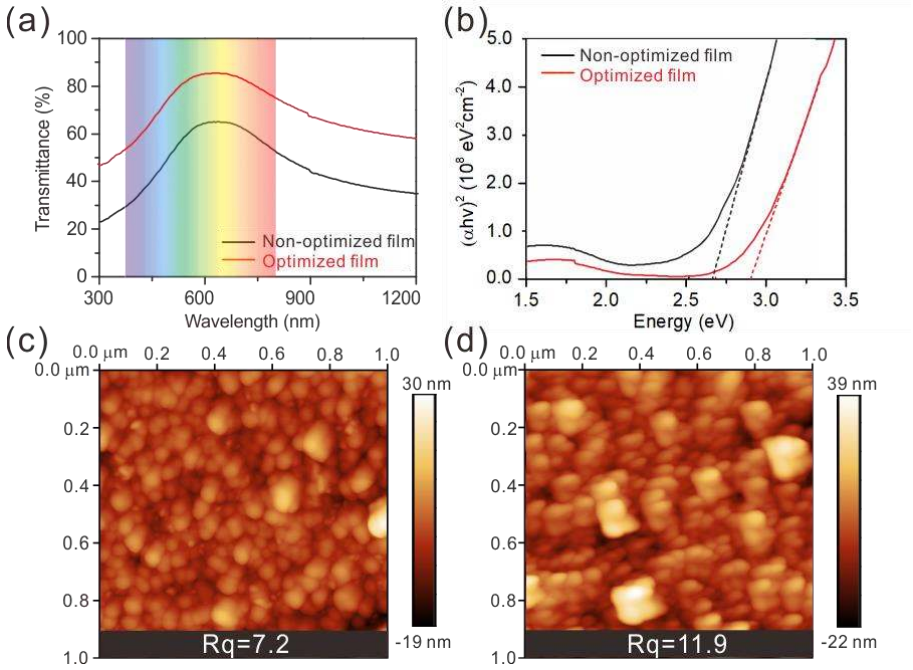

Figure 7. (a) Transmission spectra and (b) Tauc plot of optimized and non-optimized CZS films; AFM images of (c) optimized and (d) non-optimized CZS films**.**

Devices. To assess the performance of optimized and non-optimized films in optoelectronic devices, p-CZS was employed as the hole selective contact in Si heterojunction solar cells and hole transport layer in p-CZS/n-ZnO photodiodes. CZS thin films in the devices were controlled to possess almost the same thickness and reflective index. Repeat measurements (n = 15 for each PV configuration, n = 10 for photodiodes, Figures S7 and S8 and Tables S4 and S5) were performed to ensure statistical validity. Schematic structures and current density-voltage curves of devices are shown in Figure 9. For the p-CZS/n-Si and p-CZS/p^+n-Si solar cells shown in Figures 9a and b a clear enhancement in device efficiency can be observed in spite of issues with series and shunt resistance in the devices (Figure 9d and e). Optimized films with high uniformity work better to form an asymmetrical energy barrier at the heterojunction interface, allowing for low resistance collection of holes and simultaneous blocking of electrons. Better film quality (e.g. fewer pinholes) reduces shunt resistance and series resistance from the front contacts. Also, increased transparency allow for greater light absorption in the active area of the device. For photodiodes in Figure 9c, the device with optimized CZS film generates a much higher rectification ratio of 200 at $\pm$1 V bias, 30 times higher than the device with non-optimized CZS film (Figure 9f).

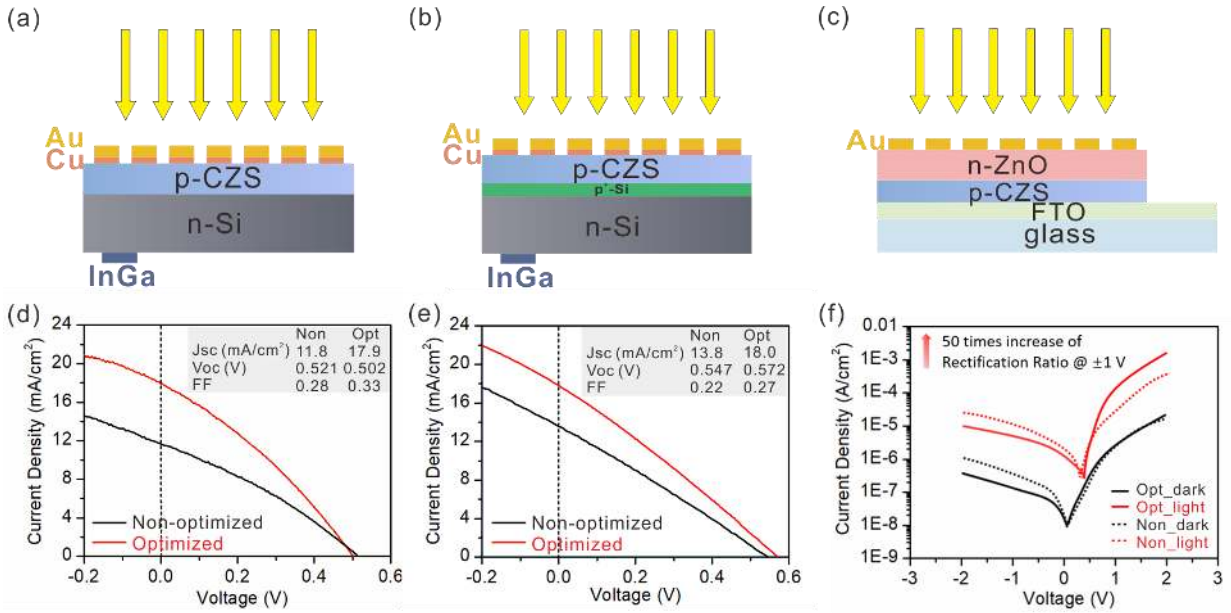

Figure 9. Schematic structure of (a) p-CZS/n-Si, (b) p-CZS/ p^+n-Si and (c) p-CZS/n-ZnO photodiodes; Photovoltaic performance of (d) p-CZS/n-Si, (e) p-CZS/ p^+n-Si and (f) p-CZS/n-ZnO photodiodes. ('Opt' represents optimized film while 'Non' represents non-optimized film)

CONCLUSIONS

Machine learning optimization in combination with design of experiment is shown to be effective in finding experimental conditions which produce p-type transparent films with high conductivity. Use of support vector regression produces a map of the chemical bath deposition synthesis space; conditions which produce peak performance can be predicted and, importantly, insights into the interactions between the deposition parameters can be obtained. Optimized p-TCM films perform well in devices such as heterojunction solar cells and photodiodes.

While the approach here could have general applicability in materials synthesis, we do need to acknowledge some limitations and challenges. We emphasize the "no free lunch" concept that no single machine learning approach is applicable to every regression problem. However, an advantage of the SVR approach taken here is that we obtain insight both from "successful" (high

FOM) and "failed" (low FOM) experiments through examination of the model's predictions. It may be possible to generalize this concept, as suggested by the proposal of Raccuglia *et al*.[87] to construct an on-line "dark reactions project" documenting experiments (failed and successful) and analyzing the outcomes using a series of regression models.

ASSOCIATED CONTENT

Supporting Information. Thermopower measurement details; Level selection and design scheme; FOMs from literature for p-TCMS; ANOVA results from first round of experiments; Statistics from the second round of experiments; Photovoltaic and photodiode device performance and statistics; support vector regression; Python code. This material is available free of charge via the Internet at http://pubs.acs.org. Python codes and datasets also available on GitHub.

AUTHOR INFORMATION

Corresponding Author

*E-mail: JWAger@lbl.gov.

Author Contributions

The manuscript was written through contributions of all authors. All authors have given approval to the final version of the manuscript.

Notes

The authors declare no competing financial interests.

ACKNOWLEDGEMENT

Chemical bath deposition and electronic characterization were performed in the Electronic Materials Program, which is supported by the Director, Office of Science, Office of Basic Energy Sciences, Materials Sciences and Engineering Division, of the U.S. Department of Energy under

Contract No. DE-AC02-05CH11231, which is supported by Division of Materials Science, Office of Science, DOE. Lawrence Livermore National Laboratory is operated by Lawrence Livermore National Security, LLC, for the U.S. Department of Energy, National Nuclear Security Administration under Contract DE-AC52-07NA27344.The authors appreciate technical support from Jilin Hu on Python programming and helpful scientific discussions from Mark Hettick, Zemin Zhang, Jiancheng Zhou and Quanhao Shen on experiments. L.F.W. acknowledges fellowship support from the Chinese Scholarship Council.

REFERENCES

(1) Ginley, D. S.; Perkins, J. D. Transparent Conductors. In *Handbook of Transparent Conductors*; 2011.

(2) Ellmer, K. Past Achievements and Future Challenges in the Development of Optically Transparent Electrodes. *Nat. Photonics* **2012**, *6*, 809–817.

(3) Varley, J. B.; Miglio, A.; Ha, V.-A.; van Setten, M. J.; Rignanese, G.-M.; Hautier, G. High-Throughput Design of Non-Oxide p-Type Transparent Conducting Materials: Data Mining, Search Strategy, and Identification of Boron Phosphide. *Chem. Mater.* **2017**, *29*, 2568–2573.

(4) Granqvist, C. G. Transparent Conductors as Solar Energy Materials: A Panoramic Review. *Sol. Energy Mater. Sol. Cells* **2007**, *91*, 1529–1598.

(5) Nagarajan, R.; Duan, N.; Jayaraj, M. .; Li, J.; Vanaja, K. .; Yokochi, A.; Draeseke, A.; Tate, J.; Sleight, A. . P-Type Conductivity in the Delafossite Structure. *Int. J. Inorg. Mater.* **2001**, *3*, 265–270.

(6) Fleischer, K.; Norton, E.; Mullarkey, D.; Caffrey, D.; Shvets, I. V. Quantifying the Performance of P-Type Transparent Conducting Oxides by Experimental Methods. *Materials (Basel).* **2017**, *10*, 1019.

(7) Stoica, M.; S Lo, C. P-Type Zinc Oxide Spinels: Application to Transparent Conductors and Spintronics. *New J. Phys.* **2014**, *16*, 055011.

(8) Asbalter, J.; Subrahmanyam, A. P -Type Transparent Conducting In2O3–Ag2O Thin Films Prepared by Reactive Electron Beam Evaporation Technique. *J. Vac. Sci. Technol. A Vacuum, Surfaces, Film.* **2000**, *18*, 1672–1676.

(9) Zhang, K. H. L.; Xi, K.; Blamire, M. G.; Egdell, R. G. P -Type Transparent Conducting Oxides. *J. Phys. Condens. Matter* **2016**, *28*, 383002.

(10) Park, S.; Keszler, D. a.; Valencia, M. M.; Hoffman, R. L.; Bender, J. P.; Wager, J. F. Transparent P-Type Conducting BaCu[Sub 2]S[Sub 2] Films. *Appl. Phys. Lett.* **2002**, *80*,

4393–4394.

(11) Hiramatsu, H.; Ueda, K.; Ohta, H.; Hirano, M.; Kamiya, T.; Hosono, H. Degenerate P-Type Conductivity in Wide-Gap LaCuOS1−xSex (X=0–1) Epitaxial Films. *Appl. Phys. Lett.* **2003**, *82*, 1048–1050.

(12) Liu, M.-L.; Huang, F.-Q.; Chen, L.-D.; Wang, Y.-M.; Wang, Y.-H.; Li, G.-F.; Zhang, Q. P-Type Transparent Conductor: Zn-Doped CuAlS2. *Appl. Phys. Lett.* **2007**, *90*, 072109.

(13) Liu, M.-L.; Huang, F.-Q.; Chen, L.-D. P-Type Electrical Conduction and Wide Optical Band Gap in Mg-Doped CuAlS2. *Scr. Mater.* **2008**, *58*, 1002–1005.

(14) Yang, K.; Ichimura, M. Fabrication of Transparent P-Type Cu x Zn y S Thin Films by the Electrochemical Deposition Method. *Jpn. J. Appl. Phys.* **2011**, *50*, 40202.

(15) Parreira, P.; Lavareda, G.; Amaral, A.; Botelho do Rego, A. M.; Conde, O.; Valente, J.; Nunes, F.; Nunes de Carvalho, C. Transparent P-Type CuxS Thin Films. *J. Alloys Compd.* **2011**, *509*, 5099–5104.

(16) Chaudhary, N.; Chaudhary, R.; Kesari, J. P.; Patra, A.; Chand, S. Copper Thiocyanate (CuSCN): An Efficient Solution-Processable Hole Transporting Layer in Organic Solar Cells. *J. Mater. Chem. C* **2015**, *3*, 11886–11892.

(17) Kudo, A.; Sekizawa, M. Photocatalytic H2 Evolution under Visible Light Irradiation on Zn1-x Cu x S Solid Solution. *Catal. Letters* **1999**, *58*, 241–243.

(18) Diamond, A. M.; Corbellini, L.; Balasubramaniam, K. R.; Chen, S.; Wang, S.; Matthews, T. S.; Wang, L.-W.; Ramesh, R.; Ager, J. W. Copper-Alloyed ZnS as a p-Type Transparent Conducting Material. *Phys. status solidi* **2012**, *209*, 2101–2107.

(19) Woods-Robinson, R.; Cooper, J. K.; Xu, X.; Schelhas, L. T.; Pool, V. L.; Faghaninia, A.; Lo, C. S.; Toney, M. F.; Sharp, I. D.; Ager, J. W. P-Type Transparent Cu-Alloyed ZnS Deposited at Room Temperature. *Adv. Electron. Mater.* **2016**, *2*, 1500396.

(20) Maurya, S. K.; Liu, Y.; Xu, X.; Woods-Robinson, R.; Das, C.; Ager, J. W.; Balasubramaniam, K. R. High Figure-of-Merit p -Type Transparent Conductor, Cu Alloyed ZnS via Radio Frequency Magnetron Sputtering. *J. Phys. D. Appl. Phys.* **2017**, *50*, 505107.

(21) Parreira, P.; Lavareda, G.; Valente, J.; Nunes, F. T.; Amaral, A.; de Carvalho, C. N. Optoelectronic Properties of Transparent P-Type Semiconductor CuxS Thin Films. *Phys. status solidi* **2010**, *207*, 1652–1654.

(22) Kang, S. R.; Shin, S. W.; Choi, D. S.; Moholkar, A. V.; Moon, J.-H.; Kim, J. H. Effect of PH on the Characteristics of Nanocrystalline ZnS Thin Films Prepared by CBD Method in Acidic Medium. *Curr. Appl. Phys.* **2010**, *10*, S473–S477.

(23) Dula, M.; Yang, K.; Ichimura, M. Photochemical Deposition of a P-Type Transparent Alloy Semiconductor Cu x Zn y S. *Semicond. Sci. Technol.* **2012**, *27*, 125007.

(24) Yang, K.; Nakashima, Y.; Ichimura, M. Electrochemical Deposition of CuxS and CuxZnyS Thin Films with P-Type Conduction and Photosensitivity. *J. Electrochem. Soc.* **2012**, *159*, H250–H254.

(25) Shin, S. W.; Agawane, G. L.; Gang, M. G.; Moholkar, A. V.; Moon, J.-H.; Kim, J. H.; Lee,

J. Y. Preparation and Characteristics of Chemical Bath Deposited ZnS Thin Films: Effects of Different Complexing Agents. *J. Alloys Compd.* **2012**, *526*, 25–30.

(26) Ortíz-Ramos, D. E.; González, L. A.; Ramirez-Bon, R. P-Type Transparent Cu Doped ZnS Thin Films by the Chemical Bath Deposition Method. *Mater. Lett.* **2014**, *124*, 267–270.

(27) Ichimura, M.; Maeda, Y. Heterojunctions Based on Photochemically Deposited CuxZnyS and Electrochemically Deposited ZnO. *Solid. State. Electron.* **2015**, *107*, 8–10.

(28) Hong, J.; Lim, D.; Eo, Y.-J.; Choi, C. Chemical Bath Deposited ZnS Buffer Layer for Cu(In,Ga)Se 2 Thin Film Solar Cell. *Appl. Surf. Sci.* **2018**, *432*, 250–254.

(29) Xu, X.; Bullock, J.; Schelhas, L. T.; Stutz, E. Z.; Fonseca, J. J.; Hettick, M.; Pool, V. L.; Tai, K. F.; Toney, M. F.; Fang, X.; Javey, A.; Wong, L. H.; Ager, J. W. Chemical Bath Deposition of P-Type Transparent, Highly Conducting (CuS)x:(ZnS)1-x Nanocomposite Thin Films and Fabrication of Si Heterojunction Solar Cells. *Nano Lett.* **2016**, *16*, 1925–1932.

(30) Schneller, T.; Waser, R. *Chemical Solution Deposition of Functional Oxide Thin Films*; Schneller, T., Waser, R., Kosec, M., Payne, D., Eds.; Springer Vienna: Vienna, 2013.

(31) Zhang, H.; Ma, X.; Yang, D. Effects of Complexing Agent on CdS Thin Films Prepared by Chemical Bath Deposition. *Mater. Lett.* **2004**, *58*, 5–9.

(32) Nemade, K. R.; Waghuley, S. A. Band Gap Engineering of CuS Nanoparticles for Artificial Photosynthesis. *Mater. Sci. Semicond. Process.* **2015**, *39*, 781–785.

(33) Kumbhojkar, N.; Nikesh, V. V.; Kshirsagar, A.; Mahamuni, S. Photophysical Properties of ZnS Nanoclusters. *J. Appl. Phys.* **2000**, *88*, 6260–6264.

(34) Prem kumar, T.; Sankaranarayanan, K. Effect of EDTA Concentration on the Physical and Optical Properties of Cds Thin Films. *Can. J. Chem. Eng.* **2013**, *91*, 27–33.

(35) Yi, G.; Lu, H.; Zhao, S.; Ge, Y.; Yang, W.; Chen, D.; Guo, L.-H. Synthesis, Characterization, and Biological Application of Size-Controlled Nanocrystalline NaYF 4 :Yb,Er Infrared-to-Visible Up-Conversion Phosphors. *Nano Lett.* **2004**, *4*, 2191–2196.

(36) Park, S. Y.; Park, J. E.; Eom, T.; Park, J. H.; Bweupe, J.; Lim, D. Characterization of ZnS Thin Films Grown Using Chemical Bath Deposition with Three Different Complexing Agents. *J. Nanosci. Nanotechnol.* **2018**, *18*, 6294–6299.

(37) Mane, R. S.; Lokhande, C. D. Chemical Deposition Method for Metal Chalcogenide Thin Films. *Mater. Chem. Phys.* **2000**, *65*, 1–31.

(38) Ortega-López, M. Improved Efficiency of the Chemical Bath Deposition Method during Growth of ZnO Thin Films. *Mater. Res. Bull.* **2003**, *38*, 1241–1248.

(39) Butler, K. T.; Davies, D. W.; Cartwright, H.; Isayev, O.; Walsh, A. Machine Learning for Molecular and Materials Science. *Nature* **2018**, *559*, 547–555.

(40) Pilania, G.; Whittle, K. R.; Jiang, C.; Grimes, R. W.; Stanek, C. R.; Sickafus, K. E.; Uberuaga, B. P. Using Machine Learning to Identify Factors That Govern Amorphization of Irradiated Pyrochlores. *Chem. Mater.* **2017**.

(41) Rajan, A. C.; Mishra, A.; Satsangi, S.; Vaish, R.; Mizuseki, H.; Lee, K.-R.; Singh, A. K. Machine-Learning-Assisted Accurate Band Gap Predictions of Functionalized MXene. *Chem. Mater.* **2018**, *30*, 4031–4038.

(42) Turcani, L.; Greenaway, R. L.; Jelfs, K. E. Machine Learning for Organic Cage Property Prediction. *Chem. Mater.* **2019**, *31*, 714–727.

(43) Oliynyk, A. O.; Adutwum, L. A.; Rudyk, B. W.; Pisavadia, H.; Lotfi, S.; Hlukhyy, V.; Harynuk, J. J.; Mar, A.; Brgoch, J. Disentangling Structural Confusion through Machine Learning: Structure Prediction and Polymorphism of Equiatomic Ternary Phases ABC. *J. Am. Chem. Soc.* **2017**.

(44) Oliynyk, A. O.; Antono, E.; Sparks, T. D.; Ghadbeigi, L.; Gaultois, M. W.; Meredig, B.; Mar, A. High-Throughput Machine-Learning-Driven Synthesis of Full-Heusler Compounds. *Chem. Mater.* **2016**, *28*, 7324–7331.

(45) Bigun, I.; Steinberg, S.; Smetana, V.; Mudryk, Y.; Kalychak, Y.; Havela, L.; Pecharsky, V.; Mudring, A.-V. Magnetocaloric Behavior in Ternary Europium Indides EuT 5 In: Probing the Design Capability of First-Principles-Based Methods on the Multifaceted Magnetic Materials. *Chem. Mater.* **2017**, *29*, 2599–2614.

(46) Singh, A. K.; Zhou, L.; Shinde, A.; Suram, S. K.; Montoya, J. H.; Winston, D.; Gregoire, J. M.; Persson, K. A. Electrochemical Stability of Metastable Materials. *Chem. Mater.* **2017**, *29*, 10159–10167.

(47) He, Y.; Galli, G. Perovskites for Solar Thermoelectric Applications: A First Principle Study of CH 3 NH 3 AI 3 (A = Pb and Sn). *Chem. Mater.* **2014**, *26*, 5394–5400.

(48) Muñoz-García, A. B.; Pavone, M. First-Principles Design of New Electrodes for Proton-Conducting Solid-Oxide Electrochemical Cells: A-Site Doped Sr 2 Fe 1.5 Mo 0.5 O 6−δ Perovskite. *Chem. Mater.* **2016**, *28*, 490–500.

(49) Cao, B.; Adutwum, L. A.; Oliynyk, A. O.; Luber, E. J.; Olsen, B. C.; Mar, A.; Buriak, J. M. How To Optimize Materials and Devices via Design of Experiments and Machine Learning: Demonstration Using Organic Photovoltaics. *ACS Nano* **2018**, *12*, 7434–7444.

(50) Gómez-Bombarelli, R.; Aguilera-Iparraguirre, J.; Hirzel, T. D.; Duvenaud, D.; Maclaurin, D.; Blood-Forsythe, M. A.; Chae, H. S.; Einzinger, M.; Ha, D.-G.; Wu, T.; Markopoulos, G.; Jeon, S.; Kang, H.; Miyazaki, H.; Numata, M.; Kim, S.; Huang, W.; Hong, S. I.; Baldo, M.; Adams, R. P.; Aspuru-Guzik, A. Design of Efficient Molecular Organic Light-Emitting Diodes by a High-Throughput Virtual Screening and Experimental Approach. *Nat. Mater.* **2016**, *15*, 1120–1127.

(51) Brandt, M.; Herbst, P.; Angerer, H.; Ambacher, O.; Stutzmann, M. Thermopower Investigation of N- and p-Type GaN. *Phys. Rev. B - Condens. Matter Mater. Phys.* **1998**, *58*, 7786–7791.

(52) Miller, N. R. Thermopower of P-Type Indium Nitride, University of California, Berkeley, 2009.

(53) Hinkelmann, K. *Design and Analysis of Experiments*; 2012.

(54) Parameswaran, R.; Box, G. E. P.; Hunter, W. G.; Hunter, J. S. Statistics for Experimenters:

An Introduction to Design, Data Analysis, and Model Building. *J. Mark. Res.* **2006**.

(55) Study, C.; Building, M. Chapter 3 Study Design and Methodology. In *Methodology*; 1995.

(56) Surowiec, I.; Vikström, L.; Hector, G.; Johansson, E.; Vikström, C.; Trygg, J. Generalized Subset Designs in Analytical Chemistry. *Anal. Chem.* **2017**, *89*, 6491–6497.

(57) Wulff, S. S. A First Course in Design and Analysis of Experiments. *Am. Stat.* **2003**, *57*, 66–67.

(58) Lu, X.; Morelli, D. T.; Xia, Y.; Ozolins, V. Increasing the Thermoelectric Figure of Merit of Tetrahedrites by Co-Doping with Nickel and Zinc. *Chem. Mater.* **2015**, *27*, 408–413.

(59) Du, B.; Li, H.; Xu, J.; Tang, X.; Uher, C. Enhanced Figure-of-Merit in Se-Doped p-Type AgSbTe 2 Thermoelectric Compound. *Chem. Mater.* **2010**, *22*, 5521–5527.

(60) Haacke, G. New Figure of Merit for Transparent Conductors. *J. Appl. Phys.* **1976**, *47*, 4086–4089.

(61) Morales-Masis, M.; De Wolf, S.; Woods-Robinson, R.; Ager, J. W.; Ballif, C. Transparent Electrodes for Efficient Optoelectronics. *Adv. Electron. Mater.* **2017**, *3*, 1600529.

(62) Jordan, M. I.; Mitchell, T. M. Machine Learning: Trends, Perspectives, and Prospects. *Science* **2015**, *349*, 255–260.

(63) Shalev-Shwartz, S.; Ben-David, S. *Understanding Machine Learning*; Cambridge University Press: Cambridge, 2014.

(64) Wolpert, D. H.; Macready, W. G. No Free Lunch Theorems for Optimization. *IEEE Trans. Evol. Comput.* **1997**, *1*, 67–82.

(65) Scott, A. J.; Hosmer, D. W.; Lemeshow, S. Applied Logistic Regression. *Biometrics* **1991**, *47*, 1632.

(66) Peterson, L. K-Nearest Neighbor. *Scholarpedia* **2009**, *4*, 1883.

(67) Ho, T. K. A Data Complexity Analysis of Comparative Advantages of Decision Forest Constructors. *Pattern Anal. Appl.* **2002**, *5*, 102–112.

(68) Tin Kam Ho. The Random Subspace Method for Constructing Decision Forests. *IEEE Trans. Pattern Anal. Mach. Intell.* **1998**, *20*, 832–844.

(69) Pedregosa, F.; Varoquaux, G.; Gramfort, A.; Michel, V.; Thirion, B.; Grisel, O.; Blondel, M.; Prettenhofer, P.; Weiss, R.; Dubourg, V.; Vanderplas, J.; Passos, A.; Cournapeau, D.; Brucher, M.; Perrot, M.; Duchesnay, E. Scikit-Learn: Machine Learning in {P}ython. *J. Mach. Learn. Res.* **2011**, *12*, 2825–2830.

(70) Mansouri Tehrani, A.; Oliynyk, A. O.; Parry, M.; Rizvi, Z.; Couper, S.; Lin, F.; Miyagi, L.; Sparks, T. D.; Brgoch, J. Machine Learning Directed Search for Ultraincompressible, Superhard Materials. *J. Am. Chem. Soc.* **2018**, *140*, 9844–9853.

(71) Smola, A. J.; Schölkopf, B. A Tutorial on Support Vector Regression. *Stat. Comput.* **2004**, *14*, 199–222.

(72) Chang, Y.; Hsieh, C.-J.; Chang, K.-W.; Ringgaard, M.; Lin, C. Training and Testing Low-

Degree Polynomial Data Mappings via Linear SVM. *J. Mach. Learn. Res.* **2010**, *11*, 1471–1490.

(73) Silverman, B. W. *Density Estimation for Statistics and Data Analysis*; Routledge, 2018.

(74) Xu, X.; Shukla, S.; Liu, Y.; Yue, B.; Bullock, J.; Su, L.; Li, Y.; Javey, A.; Fang, X.; Ager, J. W. Solution-Processed Transparent Self-Powered p-CuS-ZnS/n-ZnO UV Photodiode. *Phys. status solidi - Rapid Res. Lett.* **2018**, *12*, 1700381.

(75) Smestad, G. P.; Krebs, F. C.; Lampert, C. M.; Granqvist, C. G.; Chopra, K. L.; Mathew, X.; Takakura, H. Reporting Solar Cell Efficiencies in Solar Energy Materials and Solar Cells. *Sol. Energy Mater. Sol. Cells* **2008**, *92*, 371–373.

(76) Luber, E. J.; Buriak, J. M. Reporting Performance in Organic Photovoltaic Devices. *ACS Nano* **2013**, *7*, 4708–4714.

(77) Scholkopf, B.; Kah-Kay Sung; Burges, C. J. C.; Girosi, F.; Niyogi, P.; Poggio, T.; Vapnik, V. Comparing Support Vector Machines with Gaussian Kernels to Radial Basis Function Classifiers. *IEEE Trans. Signal Process.* **1997**, *45*, 2758–2765.

(78) Montegranario, H.; Espinosa, J. Radial Basis Functions. In *SpringerBriefs in Computer Science*; 2014; pp 69–81.

(79) Cortes, C.; Vapnik, V. Support-Vector Networks. *Mach. Learn.* **1995**.

(80) Clarke, S. M.; Griebsch, J. H.; Simpson, T. W. Analysis of Support Vector Regression for Approximation of Complex Engineering Analyses. *J. Mech. Des.* **2005**, *127*, 1077.

(81) Huang, C.-L.; Wang, C.-J. A GA-Based Feature Selection and Parameters Optimizationfor Support Vector Machines. *Expert Syst. Appl.* **2006**, *31*, 231–240.

(82) J. Weston and S. Mukherjee and O. Chapelle and M. Pontil and T. Poggio and V. Vapnik. Feature Selection for SVMs. In *Advances in Neural Information Processing Systems 13*; 2000.

(83) Golub, G. H.; Heath, M.; Wahba, G. Generalized Cross-Validation as a Method for Choosing a Good Ridge Parameter. *Technometrics* **1979**, *21*, 215–223.

(84) Efron, B. Estimating the Error Rate of a Prediction Rule: Improvement on Cross-Validation. *J. Am. Stat. Assoc.* **1983**, *78*, 316–331.

(85) Cherkassky, V.; Ma, Y. Practical Selection of SVM Parameters and Noise Estimation for SVM Regression. *Neural Networks* **2004**, *17*, 113–126.

(86) Huang, C.-L.; Chen, M.-C.; Wang, C.-J. Credit Scoring with a Data Mining Approach Based on Support Vector Machines. *Expert Syst. Appl.* **2007**, *33*, 847–856.

(87) Raccuglia, P.; Elbert, K. C.; Adler, P. D. F.; Falk, C.; Wenny, M. B.; Mollo, A.; Zeller, M.; Friedler, S. A.; Schrier, J.; Norquist, A. J. Machine-Learning-Assisted Materials Discovery Using Failed Experiments. *Nature* **2016**, *533*, 73–76.

SYNOPSIS AND TOC GRAPHIC

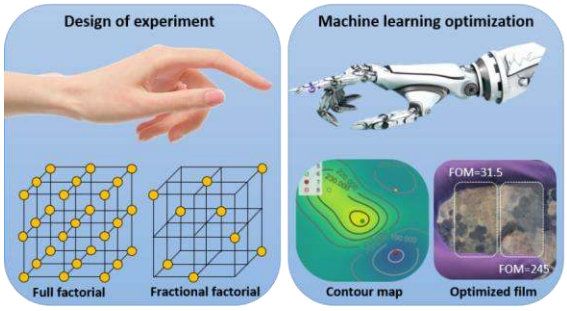

Strategic design of experiments combined with machine learning method is used to optimize the synthesis of p-type transparent conductors.